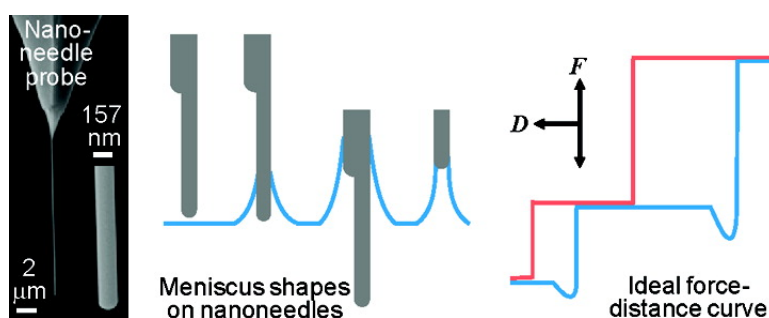


Micro-Wilhelmy and Related Liquid Property Measurements Using Constant-Diameter Nanoneedle-Tipped Atomic Force Microscope Probes

Mehdi M. Yazdanpanah, Mahdi Hosseini, Santosh Pabba, Scott M. Berry, Vladimir V. Dobrokhotoov, Abdelilah Safir, Robert S. Keynton, and Robert W. Cohn

Langmuir, 2008, 24 (23), 13753-13764 • Publication Date (Web): 06 November 2008

Downloaded from <http://pubs.acs.org> on December 9, 2008



More About This Article

Additional resources and features associated with this article are available within the HTML version:

- Supporting Information
- Access to high resolution figures
- Links to articles and content related to this article
- Copyright permission to reproduce figures and/or text from this article

[View the Full Text HTML](#)

Micro-Wilhelmy and Related Liquid Property Measurements Using Constant-Diameter Nanoneedle-Tipped Atomic Force Microscope Probes

Mehdi M. Yazdanpanah, Mahdi Hosseini, Santosh Pabba, Scott M. Berry, Vladimir V. Dobrokhotoy, Abdelilah Safir, Robert S. Keynton, and Robert W. Cohn*

ElectroOptics Research Institute and Nanotechnology Center, University of Louisville, Louisville, Kentucky 40292

Received August 7, 2007. Revised Manuscript Received September 29, 2008

The micro-Wilhelmy method is a well-established method of determining surface tension by measuring the force of withdrawing a tens of microns to millimeters in diameter cylindrical wire or fiber from a liquid. A comparison of insertion force to retraction force can also be used to determine the contact angle with the fiber. Given the limited availability of atomic force microscope (AFM) probes that have long constant diameter tips, force–distance ($F-D$) curves using probes with standard tapered tips have been difficult to relate to surface tension. In this report, constant diameter metal alloy nanowires (referred to as “nanoneedles”) between 7.2 and 67 μm in length and 108 and 1006 nm in diameter were grown on AFM probes. $F-D$ and Q damping AFM measurements of wetting and drag forces made with the probes were compared against standard macroscopic models of these forces on slender cylinders to estimate surface tension, contact angle, meniscus height, evaporation rate, and viscosity. The surface tensions for several low molecular weight liquids that were measured with these probes were between -4.2% and $+8.3\%$ of standard reported values. Also, the $F-D$ curves show well-defined stair-step events on insertion and retraction from partial wetting liquids, compared to the continuously growing attractive force of standard tapered AFM probe tips. In the AFM used, the stair-step feature in $F-D$ curves was repeatably monitored for at least 0.5 h (depending on the volatility of the liquid), and this feature was then used to evaluate evaporation rates (as low as 0.30 nm/s) through changes in the surface height of the liquid. A nanoneedle with a step change in diameter at a known distance from its end produced two steps in the $F-D$ curve from which the meniscus height was determined. The step features enable meniscus height to be determined from distance between the steps, as an alternative to calculating the height corresponding to the AFM measured values of surface tension and contact angle. All but one of the eight measurements agreed to within 13%. The constant diameter of the nanoneedle also is used to relate viscous damping of the vibrating cantilever to a macroscopic model of Stokes drag on a long cylinder. Expected increases in drag force with insertion depth and viscosity are observed for several glycerol–water solutions. However, an additional damping term (associated with drag of the meniscus on the sidewalls of the nanoneedle) limits the sensitivity of the measurement of drag force for low-viscosity solutions, while low values of Q limit the sensitivity for high-viscosity solutions. Overall, reasonable correspondence is found between the macroscopic models and the measurements with the nanoneedle-tipped probes. Tighter environmental control of the AFM and treatments of needles to give them more ideal surfaces are expected to improve repeatability and make more evident subtle features that currently appear to be present on the $F-D$ and Q damping curves.

1. Introduction

The micro-Wilhelmy method is used to determine surface tension through measurement of the force required to retract a cylindrical wire or fiber from a liquid.^{1,2} The method is used in several commercial tensiometers both for fundamental determinations of surface tension and in the development of industrial processes for coating of wires and textile fibers with diameters ranging from tens of microns to millimeters in diameter. The method is a modified version of the original Wilhelmy force balance, in which a thin plate is withdrawn from the liquid.³ However, withdrawal of the plate is subject to instabilities that can cause the meniscus to break up prior to clearly obtaining the maximum force of retraction that is identified with surface tension.⁴ The use of a Du Nouy ring in a force balance does result in a stable meniscus at maximum retraction force, and the

meniscus can be pulled some distance beyond this point prior to the ring breaking free from the liquid.⁴ Similarly, the breakup for retraction of a cylindrical fiber from liquid also occurs after the local maximum in the retraction force, leading to stable determinations of surface tension.¹

Commercial atomic force microscopes (AFMs), which have typical force detection sensitivities in the nanonewton to piconewton range, provide complete systems for recording force–distance ($F-D$) relationships over vertical scan ranges up to around 16 μm (although commercial AFM probe tips themselves are usually under 10 μm long.) The most prevalent AFM probes are tapered in shape: typically pyramidal, rather than conical. While such probes clearly detect wetting force, it can be complicated to extract surface tension from the measured $F-D$ curves. These problems include imprecise knowledge of the length of the contact line and the angle of the meniscus with the facets of the tip. While the AFM precisely reports probe height with respect to a reference surface height, additional modeling is required to determine meniscus height and shape with this complicated tip geometry. There are additional complexities in developing models to extract contact angle and

* Corresponding author. E-mail: rwohn@uofl.edu. Phone: (502) 852-7077.

(1) Dee, G. T.; Sauer, B. B. *Adv. Phys.* **1998**, *47*, 161–205.

(2) Mackay, M. E.; Carmezini, G. *Langmuir* **2001**, *17*, 1708.

(3) Adamson, A. W.; Gast, A. P. *Physical Chemistry of Surfaces*, 6th ed.; John Wiley & Sons: New York, 1997.

(4) Lapham, G. S.; Dowling, D. R.; Schultz, W. W. *Exp. Fluids* **1999**, *27*, 157.

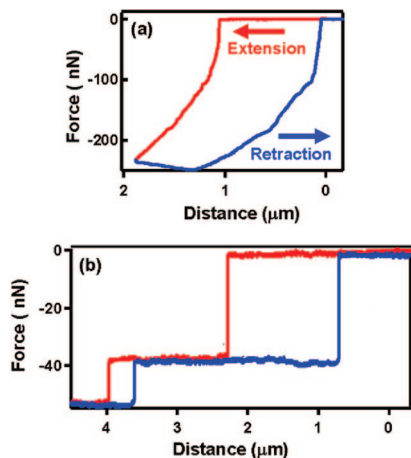


Figure 1. Comparison of F - D curves of liquids for AFM tips that are (a) standard tapered AFM tips with pyramidal cross sections and (b) constant and/or dual constant diameter (using tip 1 in Table 1). The liquid is dibasic ester measured at room temperature.

contact line length because pyramidal tips are not usually symmetric, which makes the contact line difficult to infer unless the tip shape and its angle of entry into the liquid is precisely known.

Figure 1 compares measured F - D curves for a tapered tip with a constant diameter tip for the liquid dibasic ester. For the tapered probe (Figure 1a), the F - D extension curve (red) of the probe into the liquid and retraction curve (blue) from the liquid both show a roughly parabolic shape, with near vertical curves at entry into and just prior to removal from the liquid. With increasing insertion depth, the attractive force continues to grow, corresponding to the increasing length of the contact line. This large and growing wetting force can overwhelm the cantilever stiffness and result in the unintended immersion of the cantilever into the liquid. However, for a probe that has a constant diameter tip, there is a step change in force when the tip first touches the liquid (Figure 1b). Then the force remains constant as the tip is extended until the meniscus contacts a second section of the probe that is larger in diameter. At this point in the scan, the wetting force increases again in a stepwise fashion. Therefore, a constant diameter tip has the desirable feature of maintaining a stable and constant wetting force over a range of insertion depths.

The problems with using tapered AFM probes for liquid property measurements are recognized⁵ and have led to several studies using customized tip shapes.⁶ Tipless AFM cantilevers with attached microspheres have been used to measure surface tension.⁷ Because of the high symmetry, the equilibrium meniscus height, contact line, and contact angle all can be deduced. As with the pyramidally tapered probe tips, the forces in the system vary dramatically with insertion depth. Several groups have used nearly constant diameter probe tips for measuring wetting forces on nanoscale structures,^{7,8} viscosities of liquids,⁹ and mechanical properties of living cells.¹⁰ The near constant diameter probe

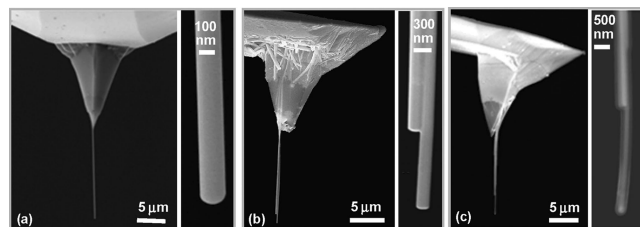


Figure 2. Types of nanoneedle-tipped AFM probes used for measuring liquid properties in this study. SEM images of (a) a constant diameter needle (tip 3, Table 1), (b) a dual-diameter needle with two fused needles each 228 nm in diameter (tip 4), and (c) a parylene-coated needle that is also dual diameter (tip 5). Insets show close-up views of the needle-tips. The tip in panel c is curved as a result of charge buildup on the insulating parylene, and the needle recovers its normally straight shape when the needle is removed from the vacuum of the SEM chamber.

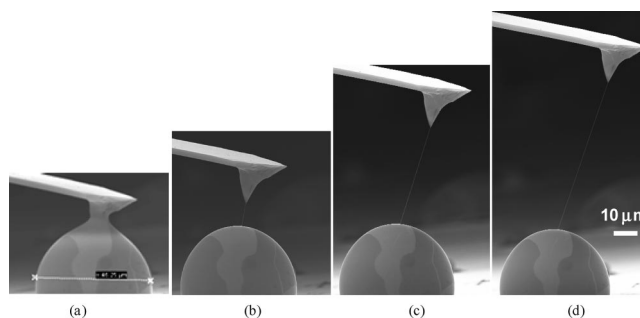


Figure 3. Time-lapse SEM images that show the growth of a Ag_2Ga nanoneedle on an AFM tip (tip 2). The images show the cantilever tip (a) first inserted into the droplet, then retracted (b) 10 μm , (c) 43 μm , and (d) 67 μm .

tips used custom-attached carbon nanotubes^{8,9} and focused ion beam (FIB) milled cylindrical probes.^{7,10} FIB probes are generally less than 4 μm long, and attached nanotubes are typically made even shorter since they tend to buckle under the slightest compressive force.¹¹ In one study, polymer cladding over most of a nanotube's length was used to reinforce against buckling.¹²

Recently, flexible metal nanowires of nearly constant diameter (that we refer to as "nanoneedles") have been selectively grown and selectively oriented on AFM probes (Figure 2).¹³ One of these needle-tipped AFM probes was used in the measurement of the F - D curve in Figure 1b, and the stepwise features are regularly seen with several liquids we have tested. The needles, which are composed of the alloy Ag_2Ga , are from a few microns up to 110 μm long and from 50 to 500 nm in diameter. A needle will begin to grow at room temperature from the surface of a silver-coated AFM probe upon inserting it into a freshly melted drop of gallium (Figure 3).^{13,14} This fabrication method is briefly reviewed in Section 4a together with a specification of the various probes used in the study. The bending and elastic buckling characteristics of these nanoneedles as they are pressed between a solid surface and the supporting AFM cantilever have been measured without breaking the needles or detaching them from the cantilever.^{14,15} These forces of buckling and detachment are

(5) Tao, Z.; Bhushan, B. *J. Phys. D: Appl. Phys.* **2006**, *39*, 3858.

(6) Jai, C.; Aime, J. P.; Mariolle, D.; Boisgard, R.; Bertin, F. *Nano Lett.* **2006**, *6*, 2554.

(7) Barrow, M. S.; Bowen, W. R.; Hilal, N.; Al-Hussany, A.; Williams, P. R.; Williams, R. L.; Wright, C. J. *Proc. - Math., Phys. Eng. Sci.* **2003**, *459*, 2885.

(8) (a) Barber, A. H.; Cohen, S. R.; Wagner, H. D. *Phys. Rev. Lett.* **2004**, *92*, 186103. (b) Barber, A. H.; Cohen, S.; Wagner, H. D. *Phys. Rev. B.* **2005**, *71*, 115443.

(9) Mechler, A.; Piorek, B.; Ratnesh, L. R.; Banerjee, S. *Appl. Phys. Lett.* **2004**, *85*, 3881.

(10) Obataya, I.; Nakamura, C.; Han, S.; Nakamura, N.; Miyake, J. *Nano Lett.* **2005**, *5*, 27.

(11) Snow, E. S.; Campbell, P. M.; Novak, J. P. *J. Vac. Sci. Technol. B* **2002**, *20*, 822.

(12) Burt, D. P.; Wilson, N. R.; Weaver, J. M.; Dobson, P. S.; Macpherson, J. V. *Nano Lett.* **2005**, *5*, 639.

(13) Yazdanpanah, M. M.; Harfenist, S. A.; Safir, A.; Cohn, R. W. *J. Appl. Phys.* **2005**, *98*, 073510.

(14) Yazdanpanah, M. M. Near room temperature self-assembly of nanostructures by reaction of gallium with metal thin films. Dissertation, University of Louisville, 2006; Chapter 8.

(15) Dobrokhotoy, V. V.; Yazdanpanah, M. M.; Pabba, S.; Safir, A.; Cohn, R. W. *Nanotechnology* **2007**, 035502.

Table 1. Specifications of the Needle-Tipped Probes Used in the Experiments

tip ID #	length (μm)	R (nm)	Δ (nm)	H (μm)
1	20	181	55	3.125
2	67	54	65	^a
3	15	78	75	^a
4	13.6	114	100	1.30
5	14.6	175 ^b	70	3.26
6	20	129	110	3.20
7	20	181 ^b	65	^a
8	9	95	90	1.97
9	10	54	50	2.50
10	14.4	75	73	3.20
11	22	80	70	^a
12	7.2	122	120	3.18
13	27	127	125	^a
14	~ 15	140	130	^a
15	~ 15	150	120	^a
16	42	181	170	^a
17	20	182	60	7.50
19	20	285	200	^a
20	22	295	270	^a
22	16	500	450	^a
23	15	503	650	^a
24	10	72	30	0.945
25	20	135	~ 100	^a
26	12.7	30	30	9.52

^a A single diameter needle. ^b Coated with 50–100 nm of parylene. Dimensions include coating thickness.

much higher than the forces encountered in the measurements of the low molecular weight, low-viscosity fluids measured herein.

In Section 2 we present an idealized model of stepwise F - D curves and show how they can be interpreted to obtain surface tension, contact angle, equilibrium meniscus height, and meniscus height at the point of maximum retraction force. Measurement of these quantities for several liquids is reported in Section 5. Additionally, the stepwise change in force provides a clear measure of the surface height of the liquid that can be used to evaluate evaporation rate, which also is reported in Section 5. A constant diameter probe also simplifies viscosity measurement over a tapered probe since the insertion depth is known and controllable, and since the expression for drag force on a cylinder is a well-known function of viscosity.¹⁶ Because the AFM scanner velocity is too low to produce adequately large drag forces, the alternative Q -damping AFM mode, where viscosity is determined through the viscous damping of the natural resonance frequency of the cantilever, is evaluated using a needle-tipped probe. This measurement method demonstrates that damping forces do increase with increasing viscosity and increasing insertion depth. However (to be described in Section 5e), the dynamic range of the measurement is limited by competition with an additional damping mechanism, which is apparent upon initial contact of the tip to the liquid, and which appears to be due to a drag or squeeze damping force of the meniscus on the sidewalls of the needle.¹⁷

This report will show that, by using constant diameter AFM probe tips, various physical properties of standard low molecular weight liquids can be measured with reasonably close agreement with published values from macroscopic measurement procedures and from macroscopic theories. While this report focuses on the degree of correspondence with macroscopic effects, given additional departures from the stair-stepped shape of the F - D curves, it appears that a number of subtle effects are also

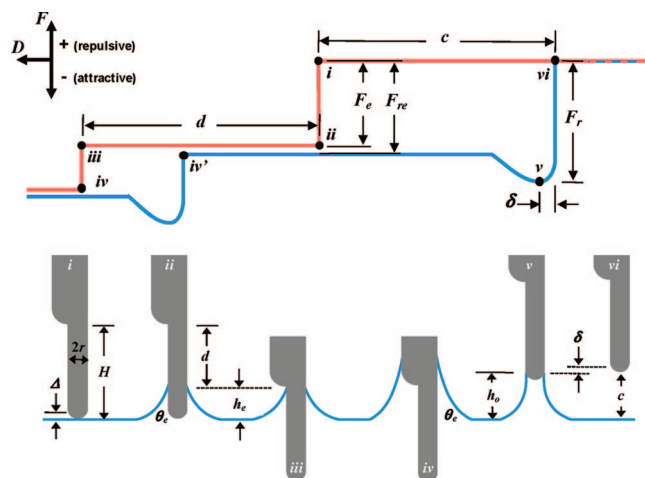


Figure 4. Idealized F - D curve of a liquid for a constant, dual-diameter needle-tipped AFM probe. Insets i - vi show the geometry of the needle and the liquid surface at the corresponding points i - vi labeled on the F - D curve. Separations between the horizontal portions of the extension and retraction curves due to differences between the advancing and the receding contact angles are assumed negligible in the idealized model as described in Section 2a, but are considered in subsequent sections and in the actual measurements.

observable and (with improved sensitivity and environmental control) could be studied using nanoneedle-tipped probes, such as dewetting dynamics, forced wetting, lubrication and plug flow, as it relates to polymer chain length entanglements, and defect pinning and contact angle hysteresis, all as reviewed by de Gennes et al.¹⁷ Additionally, the great length and small diameter of the probe tips could be useful for contacting and performing measurements on normally hard to reach individual ultrasml droplets and bubbles, such as in emulsions, and for probing ultrathin monolayer and bilayer films on liquid surfaces and at interfaces.

2. Model of the F - D Curve

This section describes the interpretation of the major features that are found on the F - D curve for the insertion and retraction from liquids of a dual diameter needle. These features are abstracted from F - D curves, e.g., the one in Figure 1b, and presented in idealized form in Figure 4. This curve is labeled with points i - vi , which correspond to insets i - vi that show the geometry of a dual diameter needle and its relationship to the liquid surface at these points on the curve. We first describe the idealized features in sequence from point i to point vi and then, following the same sequence, describe the inherent assumptions in and possible departures from this model.

a. The Idealized F - D Curve. The description of the F - D curve in Figure 4 conveniently starts with the extension scan (red curve) where the probe is in air distant from the surface (far right). The cantilever is considered to be undeflected corresponding to a zero reference force. Following the curve leftwards, the probe is extended until the tip touches the surface of the liquid at point i . As drawn, the force on the probe remains constant up to point i , which ignores slight deflections due to van der Waals forces, which, for the probes used in this study, would only result in added deflections on the order of 1 nm (see Appendix). Upon touching the surface, a meniscus spontaneously rises to an equilibrium height $h_e = h(\theta_e)$ above the planar surface of the liquid with an equilibrium contact angle of θ_e .

An expression by James¹⁸ for the height of a meniscus on a cylinder is

(16) Tirado, M. M.; de la Torre, J. G. *J. Chem. Phys.* **1979**, *71*, 2581.

(17) de Gennes, P. G.; Brochard-Wyart, F.; Quere, D. *Capillary and Wetting Phenomena*, 1st ed.; Springer: New York, 2002.

(18) James, D. F. *J. Fluid Mech.* **1974**, *63*, 657.

$$h(\theta) = r \cos(\theta) \ln \left[2.25 \frac{\kappa}{r(1 + \sin(\theta))} \right] \quad (1)$$

where θ is the angle at the contact line between the air–liquid interface and vertical. The equation also depends on r , the radius of the needle and the capillary length:^{17,19}

$$\kappa = \sqrt{\frac{\gamma}{\rho g}} \quad (2)$$

where g is the gravitational constant, ρ is the density of the liquid, and γ is the surface tension of the liquid. Numerical solutions of meniscus height by Lo²⁰ show that eq 1 gives less than 4% error in meniscus height for $r/\kappa < 0.15$ and, with submicron needle radii used in the present study and with typical capillary lengths for most liquids being of the order of 1 mm, we consider the formula to be exact.

If $\theta = 0$, which arises when discussing point v on the F – D curve, the meniscus height calculated from eq 1 is $h_0 = h(0)$. Expressing eq 1 in terms of h_0 gives

$$\frac{h(\theta)}{h_0} = \cos(\theta) \left[1 - \frac{\ln(1 + \sin(\theta))}{h_0/r} \right] \quad (3)$$

which, for $h_0 \gg r$, which we generally observe in our experiments, gives $h(\theta) \approx h_0 \cos(\theta)$.

The wetting force of the meniscus rising to its equilibrium height on the needle corresponds to the vertical distance between point i and point ii . This force is known to be

$$F_e = 2\pi r \gamma \cos(\theta_e) \quad (4)$$

where $2\pi r$ is the circumference of the air–liquid–solid contact line around the needle.

For a dual diameter needle, as illustrated in the insets in Figure 4, there is a second step change in the force between point iii and point iv due to further spontaneous wetting that occurs as the meniscus touches a wider section of the needle. Comparing inset ii to inset iii shows that the first constant diameter section (including a small rounded endcap of length Δ) is of length H and that distance d is the extension length between the stepwise changes in force between point ii and point iii on the F – D curve. Therefore, the meniscus height in inset ii can be directly determined as

$$h_e = H - d \quad (5)$$

from the horizontal scan distance d on the AFM F – D curve, together with the length H , which we measure in a scanning electron microscope (SEM; together with Δ and r).

Beyond point iv , the scan direction is reversed (moving from left to right), which is plotted as the blue curve. The F – D curve remains horizontal until the meniscus becomes pinned at the step change in diameter on the needle, causing the angle θ to decrease and causing the attractive force sensed by the cantilever to first increase, then decrease as the meniscus breaks free from the pinning point at point iv' and attaches to the smaller diameter portion of the needle. The meniscus height again is of height h_e , causing the force to return to the same value as found between point ii and point iii . Note that point iv' can appear to the left or right of point ii . The larger the ratio of the larger diameter to the smaller diameter portion of the needle, the further point iv moves to the right. Similar features occur (and are discussed in further detail momentarily)

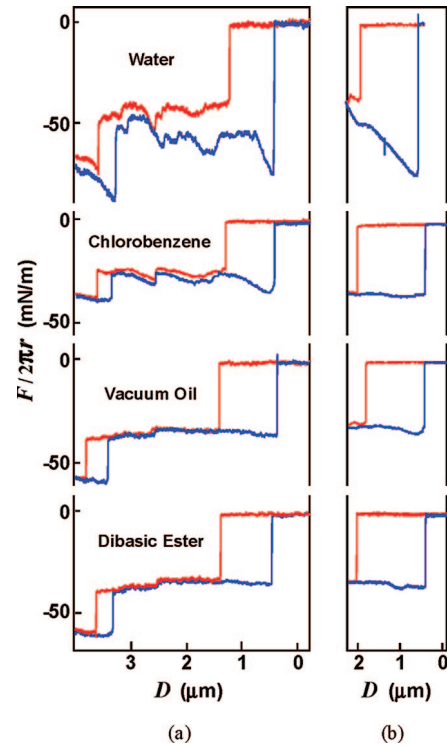


Figure 5. F – D curves for several liquids using (a) a dual-diameter (tip 6) and (b) a parylene-coated, single-diameter needle (tip 7). The difference in diameter between the two needles used in panels a and b is accommodated by normalizing the AFM force measurements by the needle circumference ($2\pi r$), which converts the vertical axis to the same units as surface tension.

Table 2. Surface Tensions of Standard Liquids Measured with Needle-Tipped AFM Probes at 22 ± 2 °C Compared with Reported Data

	Ag ₂ Ga (tip 6)		parylene (tip 7)		ref 28
	γ (mN/m)	RSD (%)	γ (mN/m)	RSD (%)	γ (mN/m)
water	74.2	1.6	72.3	2.1	72.8
chlorobenzene	33.2	2.6	34.5	3.5	33.0
vacuum oil	35.6	1.9	36.1	3.0	35.0
dibasic ester	34.1	0.9	35.7	1.2	35.6
isopropanol	24.9	1.0	24.8	1.1	23.0

for the F – D curve between point iv' (on the retraction curve) and point vi .

We have chosen to avoid using the F – D curve between point iv and point iv' for quantitative interpretation of surface tension and meniscus heights because the wider portion of the needle probe is not cylindrical, while the equations used for wetting force and meniscus height in the model of the prototypical F – D curve assume a cylindrical probe. Rather, the shape above the smaller diameter section of the needle is that of two parallel cylinders that are fused together (see Figure 2b and additional discussions on needle growth in Section 4a). This omission of data from this region of the F – D is not an issue for the development of measurement procedures, since there is sufficient additional information from the F – D curve around points v , vi , and i to determine surface tension, contact angle, h_e , and h_0 .

As the retraction scan proceeds (rightwards) from point iv' , the force remains constant until the meniscus pins on the end of the needle and the attractive force begins to increase. Point v

(19) Wong, P. K.; Wang, T. H.; Ho, C. M. *Proc. Solid-State Sens., Actuator Microsyst. Workshop* **2002**, 94.

(20) Lo, L. L. *J. Fluid Mech.* **1983**, 132, 65.

Table 3. Contact Angles of Several Liquids Measured with Ag₂Ga and Parylene-Coated Needle-Tipped AFM Probes

	contact angle with tip 6				contact angle with tip 7			
	advancing		receding		advancing		receding	
	θ (deg)	RSD (%)	θ (deg)	RSD (%)	θ (deg)	RSD (%)	θ (deg)	RSD (%)
water	59.9	1.3	48.0	3.2	61.7	2.3	49.0	2.7
chlorobenzene	42.4	4.6	36.6	5.2	19.0	4.2	17.0	5.1
vacuum oil	24.9	14.3	21.6	18.4	27.7	8.3	23.4	7.7
diabasic ester	20.6	14.6	18.6	11.6	21.6	12.4	20.0	13.9

corresponds to the position of maximum attractive force resisting the retraction of the needle. In Wilhelmy-type methods, this force,

$$F_r = 2\pi r\gamma \quad (6)$$

corresponds to the meniscus becoming parallel to the sidewall of the needle at the contact line (i.e., $\theta = 0$) and (according to eq 1) reaching a height $h_0 = h(0)$.

Usually the tips of the needles we grow are flatter than a hemisphere, i.e., their radius of curvature is greater than the diameter of the needle. Therefore we assume that the contact line is pinned¹⁷ at a distance Δ from the end of the needle (see insets i and v), where the needle begins to flatten out.

With further retraction, the force is reduced through thinning of the meniscus until the needle is retracted a distance δ beyond the point of maximum force, where the liquid bridge between the tip and the reservoir spontaneously breaks apart and the cantilever returns to the zero force position at point vi . The tip of the needle would then be found at the height

$$c = h_0 - \Delta + \delta \quad (7)$$

above the liquid. As indicated on the F - D curve in Figure 4, the scanner would need to be extended to a distance c between point vi and point i to contact the liquid. Therefore, one way to measure the meniscus height h_0 is to measure c and δ from the F - D curve and Δ from SEM images, which enable the meniscus height to be found by rearranging eq 7 as

$$h_0 = c + \Delta - \delta \quad (8)$$

b. Assumptions in the Model of the F - D Curve. In developing this model of the F - D curve, numerous simplifying assumptions have been employed. Starting with the transition between point i and point ii the deflection of the cantilever was ignored. When the meniscus rises on the needle, the wetting force also deflects the cantilever downward a distance of

$$\varepsilon_c = F_c/k \quad (9)$$

where k is the cantilever spring constant. It is this deflection, scaled by a spring constant, that is plotted as force on the vertical axis of the F - D curve. The tip position then corresponds to being slightly offset from the position of the AFM's z -scan piezomotor. In our experiments, the cantilever is sufficiently stiff to make this offset relatively small compared to the meniscus height change. In order to simplify the explanation, this small position offset, together with the cantilever offset for the transition between points v and vi , was not included in Section 2a. Correction for the offsets is presented in the Appendix, and offset-corrected results are reported for the measurements in Section 5c.

Between points ii and iii and from point iv' rightwards to the pinning point prior to point v , the F - D curves are drawn as horizontal lines of equal force. Because of the very small volume of liquid displaced by a nanoneedle, the low viscosity of the liquids studied (1–1000 cP), and the relatively low velocity of the AFM scanner (less than 100 $\mu\text{m/s}$), buoyancy and drag give negligible contribution to the force curve. The extension and

retraction curves separate if the advancing and receding contact angles differ. However, in many of our measurements, the extension and retraction curves separate only slightly, which corresponds to the idealized model that only considers a single static equilibrium angle θ_e .

In measurements, the analysis equations presented in Section 2a can be used without modification by using the advancing (or receding) contact angle in place of the equilibrium contact angle in eq 4, as long as we recognize that the numerical values of angles (and corresponding meniscus heights) can differ from each other. Therefore, unless further specified, the term *contact angle*, as well as the term *equilibrium contact angle*, will refer to the advancing contact angle in actual measurements.

Differences between the advancing and receding contact angles are usually attributed to “defects” due to chemical or shape variations on the solid surface.¹⁷ The defects can pin the triple line causing the hysteresis in contact angle. However, for defects that are small in physical dimension and low enough in modulation of the surface energy, thermal fluctuations of greater than around $20 k_B T$ can surmount the defects and attain the equilibrium height and contact angle. An example presented on page 84 of ref 17 estimates the maximum defect size that can be overcome to be on the order of 20 nm for a liquid of surface tension 20 mN/m, which decreases (with a square root dependence) to around 10 nm for a 74 mN/m liquid.

This lack of hysteresis is most closely obtained for the liquids we tested that have the lowest surface tensions. (see Figure 5 and Table 2) However, for water, which has a high surface tension, we saw not only an increased separation between the extension and retraction curves, but large vertical fluctuations that seem to suggest increased pinning by local defects on the needle.

When the needle is retracted from the liquid between points v and vi , some liquid can remain attached to the tip. The additional thickness increases the end cap thickness Δ and reduces the value of c in eq 8. Accurate modeling of the thickness of the residual liquid on the tip would be a complex problem involving consideration of a number of physical effects. As a simple estimate, we have calculated the minimal surface on a hemispherically tipped needle as it is retracted to different heights. On the basis of the shape calculated as the liquid thread begins to thin, we estimate the volume above the waist that forms a droplet on the tip. Then the minimal surface shape for the droplet is calculated, which gives the added thickness. This was calculated for a 242 nm diameter needle using values of surface tension and contact angle similar to those found in our measurements (in Tables 2 and 3). For a liquid of 35 mN/m surface tension and 20° contact angle, a lens-shaped cap 19 nm thick (and 290 zL volume) forms. For a liquid with a much higher contact angle (66°) and a surface tension of 72.8 mN/m, a droplet forms that adds 9 nm (and 2.8 zL volume) to the length of the needle.

Also, the thickness of the residual liquid is thin enough and the scan rates are slow enough (on the order of 0.1–1 s) that many liquids can evaporate substantially between points vi and i (or similarly between points ii and iii). Fortunately, the meniscus heights found in this report are 2–3 orders of magnitude larger

than these estimated thicknesses. It would be interesting to attempt to detect these subtle changes on $F-D$ curves, which would require a very sensitive and environmentally stable AFM.

The distance c can be further shortened by van der Waals forces that, just prior to point i , slightly deflect the cantilever, deform the residual liquid on the tip of the needle, and deform the surface of the liquid reservoir toward the needle. Each of these effects is estimated to be on the order of 1 nm (see Appendix).

c. Definition of Two Complementary Measurement Schemes. These equations lead to multiple schemes for determining surface tension γ , equilibrium contact angle θ_e , equilibrium meniscus height h_e , and meniscus height at maximum retraction force h_o .

In scheme 1, F_e and F_r are measured from the vertical changes in the $F-D$ curve and eqs 6, 4, and 1 are used to determine γ , θ_e , h_e , and h_o in succession.

In scheme 2, the lengths c and d from the $F-D$ curves give h_o and h_e through eqs 8 and 5. The angle θ_e could then be calculated through eq 3 and γ through eqs 1 and 2. However, because of the very slowly varying logarithmic dependence in eq 1, the solution for θ_e and γ is quite prone to errors. In order to compare the two schemes with each other, we will only compare the results for meniscus heights by the two approaches.

Note that scheme 2 requires the use of a dual-diameter needle to calculate both h_e and h_o , while scheme 1 only requires a single diameter needle to determine the four parameters. However, scheme 2 is also applicable with single-diameter needles in the determination of h_o (using eq 8). Also note that, for scheme 1, the only geometric factor that needs to be known is the needle radius r , which we measure by SEM. For scheme 2, r , H , and Δ all need to be known, and all can be measured by SEM. However, if h_o , but not h_e , is to be determined by scheme 2, then knowledge of H is not required.

In this report, we will experimentally test the model of the $F-D$ curve in two ways. The first test is to determine surface tension γ (together with θ_e) by scheme 1 and compare these values with standard accepted values of surface tension found in handbooks. The second test is to compare the values of h_o and h_e found by scheme 1 with the values of h_o and h_e found by scheme 2.

3. Related Liquid Property Measurement Principles

This section describes how constant diameter probes are well suited for the measurements of two additional liquid properties: evaporation rate χ and shear viscosity η . We note the ability to measure γ (as described in Section 2), χ , and η with a single probe, which would enable in situ determination of assorted dimensionless parameters, such as the processing parameter²¹

$$P = \eta\chi/\gamma \quad (10)$$

P is well correlated with the rate of *capillary thinning* of liquids, e.g., the thinning of the liquid thread that forms when the needle is pulled past point v in Figure 4. Much larger values of P , corresponding to polymeric solutions with much higher viscosities than were considered in this study, predict stable fiber formation in fiber drawing and electrospinning.^{22–25} The ability to measure

P in situ with a single probe could prove useful for process control of nanomanufacturing with the same needle used as a brush or stylus, e.g., for transfer of small droplets of controlled volumes from the tip to a surface, or for point-to-point drawing of nanofibers.^{22,24}

a. Evaporation Rate. Figure 6 shows $F-D$ extension curves for a dual-diameter needle that is repetitively inserted and withdrawn from the volatile solvent chlorobenzene. The stair-step features are clearly seen in each curve, and from these features the change in surface height l per scan repetition period t can be related to evaporation rate χ (in units of volume loss/surface area/time). If the surface is planar,

$$\chi = l/t \quad (11)$$

However, in our studies, we find it easier to insert the needle into the liquid if the liquid protrudes above the lip of a small (1 cm diameter) container. In this arrangement, the radius of curvature of the cap changes, rather than the height of the cylindrical column of liquid. Consideration of this specific geometry leads to

$$\chi = l/2t \quad (12)$$

which is accurate to within 2% for caps that protrude above the container less than 10% of the radius of the container.

b. Shear Viscosity. Viscous drag force F_d on a slender cylindrical rod is proportional to flow rate v for low flow rates corresponding to a Reynolds number less than 1. The proportionality for flow parallel to the axis of a cylinder of radius r is¹⁶

$$R = \frac{F_d}{v} = \frac{2\pi\eta L}{\ln(L/2r) - 0.2 + 1.8r/L}; \quad L \geq 4r \quad (13)$$

where, for our measurements, L represents the insertion depth of the nanoneedle into the liquid, and v corresponds to the AFM scanner speed. Equation 13 is nearly linear with insertion depth L , with only slight departures from linearity due to the denominator term. Similarly, the equation is only weakly dependent on radius.

With the maximum vertical scan rate of our AFM being around 100 $\mu\text{m/s}$ (which is typical of commercial AFMs), the drag force produced is near the limit of detection of the AFM. For example, a needle of radius $r = 200$ nm inserted to a depth of $L = 16$ μm produces a drag force of 4.7 pN/cP at the maximum scan velocity.

The limit of detection is set by the thermal noise in the AFM detector circuitry, which is set by thermal vibration of the cantilever and the detector electronics themselves. Several AFMs provide access to the noise signal. For our AFM, the noise equivalent amplitude fluctuation of the cantilever is on the order of 0.1 nm, depending somewhat on the cantilever used. The amplitude multiplied by the cantilever spring constant gives the minimum detectable force, which is observed as noise fluctuations in force on the $F-D$ curves (e.g., in Figure 5). For the cantilevers used in this study, the spring constants are from 2 to 5 N/m, and the measured noise equivalent fluctuation amplitude is 0.085 nm, giving a force detection limit of 170 to 425 pN and a viscosity detection limit of 36 to 90 cP, which is well above the viscosities of several liquids evaluated herein. Also, as described in Section 5a, scan speeds lower than 100 $\mu\text{m/s}$ actually were required to obtain the most stable $F-D$ curves. In passing, we note that drag force sensitivity for the softest commercially available cantilevers have spring constants of 0.01 N/m and an estimated fluctuation amplitude of 0.06 nm, which would lead to a viscosity detection limit of ~ 0.13 cP at a 100 $\mu\text{m/s}$ scan speed.

Because of the limited sensitivity of the linear drag force measurement method for low viscosity liquids, we instead measure

(21) Tripathi, A.; Whittingstall, P.; McKinley, G. H. *Rheol. Acta* **2000**, *39*, 321.

(22) Harfenist, S. A.; Cambron, S. D.; Nelson, E. W.; Berry, S. M.; Isham, A. W.; Crain, M. M.; Walsh, K. M.; Keynton, R. S.; Cohn, R. W. *Nano Lett.* **2004**, *4*, 1931.

(23) Pabba, S.; Sidorov, A.; Berry, S. M.; Yazdanpanah, M. M.; Keynton, R. S.; Sumanasekera, G.; Cohn, R. W. *ACS Nano* **2007**, *1*, 57.

(24) Berry, S. M.; Harfenist, S. A.; Cohn, R. W.; Keynton, R. S. *J. Micromech. Microeng.* **2006**, *16*, 1825.

(25) Keun, S. W.; Youk, J. H.; Lee, T. S.; Park, W. H. *Polymer* **2004**, *45*, 2959.

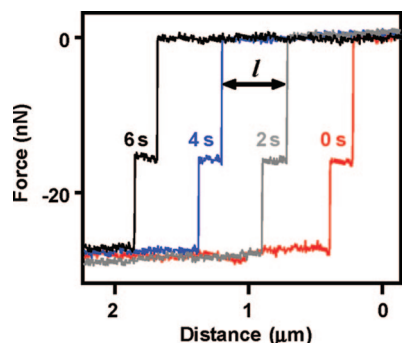


Figure 6. F – D extension curves of chlorobenzene repeated every 2 s using tip 24.

viscosity through the changes to the cantilever vibration spectrum caused by viscous damping. The cantilevers have a fundamental vibration frequency of around 70 kHz with a quality factor in air of $Q = 200$. The AFM has a specific mode that automatically evaluates the Q of the cantilever resonance from its measurements of the thermally excited spectrum.²⁶ If a needle-tipped cantilever is inserted into a liquid, the Q of the resonance decreases to

$$Q = \sqrt{Mk}/R \quad (14)$$

where M is the effective mass of the cantilever, and k is the cantilever spring constant. From eqs 13 and 14, Q can be related to viscosity η as

$$\frac{1}{Q} = \frac{1}{\sqrt{Mk}} \frac{2\pi\eta L}{[\ln(L/2r) - 0.2 + 1.8r/L]} \quad (15)$$

Equation 15 has two unknowns: Q and M . A calibration is required to determine the value of M . This is done by measuring Q for a reference liquid of known viscosity and solving eq 14 for M .

Since this measurement method is performed with extremely small vibration amplitudes compared to the meniscus heights, contact angle (and hence, wetting force) can barely change during the oscillation. As a result, we have assumed that the wetting force essentially provides a constant tension that does not affect the measurement of damping changes. However, in actual measurements, corrections for additional sources of damping (e.g., air damping of the cantilever and a surface damping effect—to be discussed in Section 5e,) may need to be included as well. Since the value of L can be varied, we will use the slope of eq 15 for large insertion depths to distinguish damping due to drag force from other sources of damping.

4. Experimental Methods

a. Growth of Needle Tips on AFM Probes. This section briefly reviews the method of growing the nanoneedles on AFM cantilevers, in addition to providing details on the specific geometric features of and material modifications to the needles used in this report.

Figure 3 shows time-lapse SEM images of the growth of one of the longest, individually grown Ag_2Ga nanoneedles made to date. The cantilever being manipulated is in an SEM, but acceptable needles for this study have also been grown in air using an M5 AFM (Veeco, Santa Barbara, CA) in which the stage stepper motors and video microscope optics are used to control the insertion of the cantilever into the gallium. The needle is grown and oriented with respect to the cantilever by the method of Yazdanpanah et al.¹³ First, the cantilever underside and tip are sputter-coated with silver to a film thickness of 50–150 nm. Generally, the thicker the coating, the longer the needle produced. Also note that needles have been

successfully grown from sputter-deposited films from two different sputterers, but to date, no needles have been observed to grow from films deposited by thermal or e-beam evaporation.

A melted drop of Ga (diameter typically 5–100 μm) is placed on a glass, oxide free silicon, or thinly oxidized silicon wafer. Then the Ga is etched in 1 N HCl at 60 $^\circ\text{C}$ to remove any native oxide. This last step causes the droplet to take on a spherical shape. However, needles form equally as well when a flattened, irregularly shaped droplet (due to the presence of the subnanometer thick oxide) is used.^{13,14} While Ga melts at 29.15 $^\circ\text{C}$, it can remain melted, or *supercooled*, to temperatures well below room temperature. The needles used in this study were grown at room temperature.

The nanoneedles are grown by inserting the tip of the Ag-coated AFM cantilever 1–4 μm into a Ga droplet, then retracting the cantilever slightly to form a meniscus on the tip (Figure 3a). Silver solute dissolves from the tip up to the air–liquid–solid contact line. The Ag supersaturates the Ga solvent, and then the Ag and Ga nucleate and grow one or more needle-shaped crystals of the intermetallic alloy Ag_2Ga on the area at the end of the tip, which has just been cleared of silver by dissolution.

Once needle growth in the Ga droplet begins, the needles continue to grow, and, eventually, a single needle grows past all the other needles. The growth rate for single needles has been observed to be between 0.1 and 2 $\mu\text{m}/\text{s}$. The growth can continue all the way through the gallium to the substrate. Even longer needles can be produced (Figure 3b–d) if the cantilever is retracted, which does not appear to change the growth or the diameter of the needle. The retraction speed, which is controlled through the nanomanipulator joystick, was about 500 nm/s to distances of about 6 μm before the retraction was paused to capture an SEM image.

Nanoneedles have been grown in as little as a few seconds, but typically a few minutes are required for the operator to experimentally determine the correct insertion depth for growth to start. The insertion depth determines how much Ag is dissolved into the liquid Ga and, consequently, the degree of supersaturation within the Ag/Ga mixture. Therefore, insertion depths are kept small to avoid extreme oversaturation, which reduces the number of needles that initially are nucleated at the start of growth. The combined procedure of cantilever insertion, dissolution, nucleation, and growth usually is completed in less than 5 min. Needles are faceted, having a cross section that can have 8–16 sides. We consider this cross section to be nearly cylindrical since the circumference of a circle is only 2.5% greater than that of an inscribed octagon.

The needles appear to be directed to grow along the longitudinal axis of the meniscus. This feature is used to produce needles of desired orientations with respect to the cantilever. For liquid property measurements reported herein, the needles are intentionally grown at 12 $^\circ$ with respect to the cantilever declination, which results in a needle that is oriented perpendicularly to horizontal in the MFP3D-SA AFM (Asylum Research, Santa Barbara, CA) that is used in this study. SEM observations show that most needles, and all needles used in this study, deviate by less than 3 $^\circ$ from the desired perpendicular direction.

To date, needles have been fabricated with lengths ranging from 1 to 110 μm and diameters from 25 nm to 1.1 μm .^{13–15} For the measurements of liquid properties reported here, the diameters of single needles were from 108 to 1006 nm, which are listed individually in Table 1 together with relevant geometrical parameters.

During the fabrication procedure needles frequently are found to grow as fused pairs, with one needle eventually growing past the other. In several experiments it was possible to observe a single needle beginning to grow past the other and quickly remove the needle from the Ga producing a dual diameter needle with a short single diameter region of length H between 1 and 4 μm . Removing the needle with a somewhat longer delay results in a longer needle. Eleven of the 26 probes used in this study (listed in Table 1) have dual diameters.

Two needles used in liquid property measurements (tips 5 and 7, Table 1) were surface modified with the organic vapor-deposited polymer parylene. The conformal coating was deposited using a PDS 2010 coater (Specialty Coating Systems, Indianapolis, IN).

(26) Hutter, J. L.; Bechhoefer, J. *Rev. Sci. Instrum.* **1993**, *64*, 1868.

(27) Israelachvili, N. *Intermolecular and Surface Forces*, 2nd ed.; Academic Press: San Diego, CA, **1992**; pp 152–192.

Figure 2 shows SEM images of standard AFM probes on which needle tips have been grown that are (a) constant diameter, (b) dual diameter, and (c) parylene coated. The parylene coated needle is also dual diameter.

b. Methods Common to All the AFM Measurements of Liquid Properties. As mentioned in Section 4a, an MFP3D-SA AFM was used for all $F-D$ and Q -damping measurements. All AFM cantilevers used in this report are BS-Multi75 (Budget Sensors, Sofia, Bulgaria) with a resonance frequency of 75 ± 15 kHz, a spring constant of 2–5 N/m, and Q (in air) between 180 and 220. The exact values of these parameters are individually measured in the same AFM that is used to measure the liquid properties.

Except for the Q -damping measurements, which do not produce $F-D$ curves, $F-D$ curves are recorded for repetitive scans rates of 0.01–4 Hz and scan ranges from 3 to 16 μm (corresponding to linear scan velocities of 0.030–64 $\mu\text{m/s}$). The measurement of evaporation rate is performed at the center of an aluminum pan (1 cm diameter, 2 mm high) where the surface of the liquid is highest. For measurements of surface tension, contact angle, and viscosity, the $F-D$ curves are more stable if the needle is positioned close to (~ 100 μm from) the edge of the pan. For these measurements, the pan is slightly overfilled as viewed in profile by the eye. The surface at the very edge of the pan is no more than 5° from level. With a needle tilt of 3° , the needle is normal to 8° worst case, but the tilt would typically be expected to be much less than this.

The spring constant k for each cantilever is measured using the thermal noise method.²⁶ The calibration is completed by measuring the change in the photodetector signal as the needle-tipped cantilever is pressed against a rigid surface. Note that the applied force is sufficiently small such that the needle does not bend or buckle¹⁵ during this part of the calibration, as well as in subsequent measurements. Once the values of k and the calibration constant are determined in this way, the AFM software is calibrated to accurately report force versus distance.

The needles are imaged with a Supra 35 SEM (Zeiss, Oberkochen, Germany) which has ~ 2 nm resolution. The needles are imaged from two different perspectives before and after each experiment to confirm that there is no residual material or damage to the needles. If any residue is observed on a needle, it is washed by immersing the probe in a bath of acetone for 2–5 min.

Several measurements of several liquids were performed both with Ag_2Ga - and parylene-overcoated needles. All measurements were done under standard laboratory conditions with an average temperature of 22°C with a long-term variation of $\pm 2^\circ\text{C}$ over the duration of the study. The building heating and cooling system is set to maintain relative humidity at around 30–35%.

5. Experimental Evaluation of the Measurement Methods

This section reports the values of surface tension (together with contact angle and meniscus height), evaporation rate, and viscosity of various liquids that were measured using the needle-tipped probes. The measured values are compared against values from the published literature or from traditional measurement procedures that we performed on the identical liquid samples.

a. Scheme 1: Surface Tension. Surface tension for the various liquids is determined from eq 6 using the retraction force F_r found from measured $F-D$ retraction curves (the difference in force between point v and point vi in Figure 4) and needle radius measurements from SEM examination. $F-D$ curves for four liquids are presented in Figure 5 for $F-D$ scans at a speed of 1.5 $\mu\text{m/s}$ with an uncoated dual diameter needle and with a single-diameter parylene-coated needle. As mentioned in Section 2b, the horizontal regions of each scan in Figure 5a show a similar deviation toward the midpoint of distance. This corresponds to the position of a small structural defect on the needle, which introduces a noticeable pinning force.

Some experimentation was required to identify the preferred scan speed. $F-D$ scans similar to those in Figure 5 were

repetitively recorded. At low velocities of 0.01–1 $\mu\text{m/s}$, the force curves did not repeat themselves and usually shifted over time as a result of evaporation of the liquid and thermal drift of the AFM. At high velocities of 20–100 $\mu\text{m/s}$, the force curves became less stable, and the stepwise changes in the force curves became less clear. Scan velocities of 1–15 $\mu\text{m/s}$ gave the most stable readings. Within this range, we have not observed appreciable variations in the values of F_r . For each liquid, 20 $F-D$ curves were recorded (with scan velocities of 1, 5, and 15 $\mu\text{m/s}$) from which F_r was measured and the average value and standard deviation of γ was calculated. The average and relative standard deviation (RSD; i.e., the standard deviation divided by average) are reported in Table 2 for each liquid measured using an uncoated needle and a parylene-coated needle.

The repetitive measurements of surface tension give values with RSDs of 3.5% or less for all values in Table 2. Ideally, surface tensions measured using the coated and uncoated needles should be identical and the relative difference (RD) between the measurements were less than 4.7% for the five liquids that were measured with both needles. The RDs for the 10 measured values of surface tension are from 4.4% below to 8.3% above the published values for surface tension. We have not been able to further resolve these discrepancies, which could arise from a number of physical factors, as discussed in Section 2b, and any errors in measuring the circumference of the needle, as discussed in Section 4a.

b. Scheme 1: Contact Angle. Contact angle is evaluated from the values of F_e and F_r as measured from $F-D$ curves (the identical curves from Section 5a), followed by calculation of θ_c using eqs 4 and 6. With contact angle hysteresis being evident (as discussed in Section 2b), we associate F_e with the advancing contact angle, and F_{re} with the receding contact angle (see Figure 4). In our evaluation of the experimental $F-D$ curves (e.g., in Figure 5), we specifically choose to measure F_e as the difference in force between point i and point ii directly in the vicinity of these two points. This method of measuring the force was deemed preferable to trying to estimate the average height of the nearly horizontal line between points ii and iii . Similarly, the receding force F_{re} is measured on the retraction curve, directly below points i and ii . While further evaluation of the most accurate way to evaluate the curves is in order, it is satisfying to note that the values of force measured in this way generally gave reasonably similar values from scan to scan. The values of contact angle measured in this way are reported in Table 3. The standard deviations of the contact angles vary from 0.8 to 4° (corresponding to the RSDs from 1.3 to 18.4% in Table 3.) The larger deviations correspond to a loss in numerical sensitivity related to calculating the contact angle from eqs 4 and 6 as

$$\theta_c = \cos^{-1}(F_e/F_r) \quad (16)$$

For instance, at 60° a deviation of -4° corresponds to a difference in the ratio of F_e/F_r of 0.06 (or a 12% RD between the ratios of forces.) However, for a 20° contact angle, an error of -4° gives a difference of 0.022 (or 2.3% RD between the ratios.) Therefore, as the contact angle decreases, the differences between F_e and F_r become smaller and increasingly hard to differentiate from $F-D$ curves, which tend to magnify errors in the measurements of contact angle.

Since Ag_2Ga is not available as a planar coating, but parylene is, we measured the contact angle of glass microscope slides that we coated with ~ 50 nm of parylene, at the same time we coated the needle used in contact angle measurements. The slides were inserted perpendicular to the surface of the liquid and the static contact angle was viewed and digitally captured with a video

Table 4. Comparison of Meniscus Heights Determined by Scheme 1 and Scheme 2^a

measured heights using tip 8	h_o			h_e		
	scheme 1 (nm)	scheme 2 (nm)	RD (%)	scheme 1 (nm)	scheme 2 (nm)	RD (%)
water	1053	1048	-0.5	470	416	-13
chlorobenzene	1009	1041	3.1	709	998	29
vacuum oil	1025	1015	-0.9	899	943	5.7
dibasic ester	1023	1088	6.0	831	922	10

^a Tip 6 was used for the scheme 1 determination by eq 1 and tip 8 was used for the scheme 2 determination by eqs 5a and 8a.

microscope and CCD camera. The conditions of immersion appear to be most closely related to the *equilibrium* contact angle. The measured angles are 72.0, 18.5, 22.0, and 29.5 ° for water, chlorobenzene, vacuum oil, and dibasic ester, respectively. Vacuum oil and chlorobenzene have contact angles that are quite close to the AFM-measured angles, while the macroscopically measured values for dibasic ester and water are noticeably larger than the AFM-measured advancing angle.

c. Meniscus Heights Using Scheme 2. Values for c , d , and δ as identified in Figure 4, are found from F - D curves measured in the same way as in Sections 5a and 5b, this time using tip 8, which is uncoated Ag_2Ga . The values of these three parameters were taken from five F - D curves at scan speeds of 0.5, 1.5, 3, 4, and 5 $\mu\text{m/s}$ (which showed no appreciable differences). The values of h_e and h_o are then found by application of eqs 5a and 8a from the Appendix, which are modified from eqs 5 and 8 to account for height changes caused by offsets in the tip height due to cantilever bending. The values of meniscus heights are calculated for each scan speed, and then the average value of height is reported in Table 4. Table 4 compares the resulting values with the meniscus heights calculated by scheme 1 (where the heights are calculated by eq 1 using the values from Tables 2 and 3 as measured with tip 6). The correspondence between the heights by the two schemes appears to be generally closer for measurements of h_o than for h_e . The smaller deviations between the two schemes for h_o is likely due to the fact that the equation for h_o only depend on one measured parameter γ (and an assumed contact angle of 0°), while the equation for h_e depends on measurements of both surface tension and contact angle. More precise measurements are required to determine if these deviations in meniscus height between the two schemes might be due to factors other than measurement errors, such as those secondary factors discussed in Section 2b.

An additional comparison of meniscus height h_o by the two schemes was performed as a function of radius for a single liquid (water). Ag_2Ga needles of 15 different diameters (tips 9–23) were used. The parameters c and δ are measured from 10 F - D curves taken from scan speeds of 0.5 to 5 $\mu\text{m/s}$, h_o is calculated by eq 8a for each scan, and the averaged value of h_o is plotted in Figure 7. The RSD of h_o for the 10 scans from one tip is less than 1%. The meniscus heights for scheme 1 (again calculated from eq 1 using the AFM-measured values from Tables 2 and 3) is plotted against the scheme 2 values of h_o for the 15 needles. For comparison, the values for h_e (as well as h_o) for water from the F - D curves from tip 6 (used to derive Tables 2 and 3) and tip 8 (used to derive Table 4) are also plotted in Figure 7a. The measurements of h_o by scheme 2 roughly follow the scheme 1 curve. A least-squares fit of the scheme 1 model with a single free parameter of vertical offset produces the dashed line. It is offset by -295 nm and the standard deviation is 251 nm. Figure 7b replots the scheme 2 data as h_o/r , the meniscus height normalized by the radius of the needle, to enable visual comparison of the meniscus height for different scale sizes. The dashed line

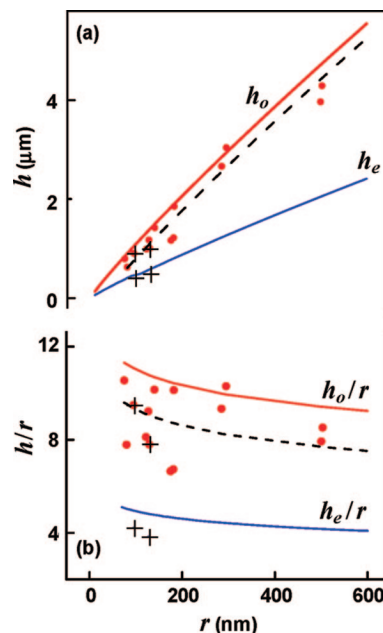


Figure 7. Comparison between the values of (a) meniscus height h_o and (b) h_o/r of water for the two schemes. Scheme 1 results are plotted as a continuous curves, and scheme 2 is plotted as data points for needles of various radii (tips 9–23). The dashed curves are the scheme 1 curves offset by an amount that minimizes the mean square error between the scheme 1 curve and the scheme 2 data. Additional data points (shown by the symbol “+”) for both h_o and h_e are calculated by scheme 2 from the F - D curves for the dual diameter probes tips 6 and 8. These are included to allow comparison with the scheme 1 calculation of h_e .

shows the scheme 1 model (as determined by a least-squares fit) with an offset of -1.72 and a standard deviation of 1.32 (~15% RSD). The widest fluctuations in h_o/r appear to occur for needle radii that are less than 200 nm.

d. Evaporation Rate. Evaporation rate for several liquids was determined from eq 12 by using the measured change in the height l from successive F - D retraction curves of known scan period t . The value of l is measured 10 to 20 times from consecutive F - D scans. The scan range is between 5 and 16 μm at scan rates between 0.01 and 25 Hz depending on the evaporation rate of the liquid. The more rapid the evaporation rate, the faster the scan rate, and the longer the scan ranges need to be.

Thermal drift in the vertical scan height can be a concern in AFM measurements. But we find that with care in allowing the temperature to stabilize, that quite slow changes in surface height can be measured without resorting to advanced temperature regulation methods. We specifically characterized drift of the AFM system immediately prior to measuring evaporation rate by recording the F - D curve of the same glass microscope slide that supports the liquid sample holder. For rapidly evaporating liquids, evaporation rate measurements are usually performed immediately after loading the liquid in the AFM. The drift rate at this point in time is ~5 nm/s, which is caused by the temperature of the sample holder equilibrating with the AFM. However, this is an acceptably small level of drift for liquids that evaporate much faster than this rate. Given at least 30 min to equilibrate, the drift is found to be around 0.16 nm/s, which is suitable for more slowly evaporating liquids. For low evaporation rates, the sample can be loaded several hours before the measurements, and drifts of around 0.020 nm/s are obtained. In all cases reported in Table 5, drift was small or negligible compared to the evaporation rate. Working within these limits,

Table 5. Evaporation Rates Measured by AFM with Tip 25 Compared with Values Measured by TGA

	AFM				TGA
	χ (nm/s)	RSD (%)	drift (nm/s)	scan rate (Hz)	χ (nm/s)
acetone	1450	2.0	5	16	1020
isopropanol	320	3.2	5	16	178
chlorobenzene	110	4.0	5	16	98
water	27	3.0	0.16	1	36
dimethyl formamide	11.5	2.6	0.16	0.5	9.4
dibasic ester	0.30	15	0.02	0.01	0.22

we were able to measure an evaporation rate for dibasic ester of 0.30 nm/s from 20 successive measurements of l taken over 33 min. As shown in Table 5, this measurement has an RSD of 15%, which is the largest deviation of any measurement. This corresponds to the dibasic ester measurement having the largest relative drift rate (drift rate/evaporation rate) of the liquids measured, 15%.

As a comparison, the identical liquids were measured by a thermogravimetric analyzer (TGA) (TA 2050, TA Instruments, New Castle, DE). The instrument records the weight of a sample as a function of time. From the density of the liquid and the surface area of the sample exposed to air, the evaporation rate is calculated. The samples are measured in a chamber regulated at 25 °C. The results for TGA are included in Table 5 and differ by 11–45% from the AFM data. It is likely that these discrepancies can be reduced by precise regulation of the relative humidities and temperatures of the two laboratories where the AFM and TGA are located. Nonetheless, evaporation rates measured with the needles track well over several orders of magnitude.

e. Shear Viscosity. The viscosity of aqueous solutions of glycerol (0–99.5 wt %) is measured using the Q -damping method described in Section 3b. A single parylene coated needle (tip 7) is used in each measurement. The needle is first inserted to a maximum distance (around 7–16 μm with smaller distances used for more viscous solutions), and then Q is measured. The needle is retracted in steps, making a new measurement of Q at each depth. The zero value of insertion depth is referenced to the distance at which the needle breaks free from the liquid (point vi in Figure 4), leaving it at a height of $\sim c$ (see eq 7 above the surface). Because the retraction in the Q -damping mode is done in discrete steps of around 0.1 μm and because the AFM does not provide F – D measurements during retraction, there can be an error in the zero reference of around 0.1 μm . There are also several ambiguities in insertion depth L due to the rounded endcap of length Δ , which is not accounted for in the drag force model, changes in insertion depth due to stretching of the meniscus on retraction, and changes in surface height due to evaporation (which is reduced by insertion of the probe close to the edge of the slightly overfilled pan). These ambiguities have led us to estimate the shear viscosity based on fits to the slope of eq 13 at large insertion depths, rather than performing a regression to eq 15. This type of fit as a function of change in length also allows the damping due to drag force to be discriminated from other damping factors, including the air damping of the cantilever and a surface damping term that is observed in the measurements presented in Figure 8.

Figure 8a shows the estimated viscosities that were derived from the $1/Q$ versus L curves plotted in Figure 8b,c. The

experimental data in Figure 8b,c are also annotated with the slopes that were used to calculate the relative viscosities of the solutions. The reference liquid is chosen to be the 60 wt % glycerol solution. For this arbitrary choice of reference liquid, the very lowest and highest concentrations of the solutions give overly low values of viscosity as compared to published values²⁸ and our own measurements of identical solutions at laboratory temperatures between 21 and 23 °C (using a Brookfield LV-DV II+ cone-and-plate viscometer at shear rates from 1350/s for pure water down to 1.5/s for pure glycerol).

The data in Figure 8b,c show some of the limitations of the Q -damping method. For pure water, the data are very widespread, making a unique slope difficult to determine. Also, the damping $1/Q$ is not much different than the cantilever damping in air, even for the largest insertion depths. For 99.5 wt % glycerol, the damping increases to more than 0.5 ($Q < 2$) before the needle is inserted its full length. The mechanical response is only slightly resonant at such low values of Q , making practical measurement of Q difficult.

Additionally, there is a viscosity-dependent damping term that is present, even when the needle is less than a micron from breaking free from the liquid. This surface damping factor, for the more viscous liquids, can substantially reduce Q below that of the air damping of the cantilever, thereby reducing dynamic range of the measurement of drag force.

We believe that the source of the surface damping is due to large shear rates across the very thin channel between the sidewalls of the needle and the air–liquid interface of the meniscus, which would be greatest near the triple line. A model of this source of dissipation (in ref 17, p 143) can be adapted to the geometry of the needle and gives a drag ratio (analogous to Stokes drag in eq 13) of

$$R_m = \frac{F_m}{\nu} = 2\pi r \frac{3\eta \ln(h/a)}{\theta} \quad (17)$$

for a contact angle with the sidewall θ , a length h that is length of the meniscus in contact with the needle sidewall, and a molecular cutoff length a (typically chosen as 1 nm), which is used to avoid a singularity in the solution method. For a needle inserted to a depth greater than the equilibrium meniscus height h_e , the height $h = h_e$, and the value of R_m is constant. For a large insertions depth, the ratio of the damping due to the meniscus $1/Q_m$ compared to damping due to Stokes drag on a cylinder (from eqs 13 and 15) is approximately

$$\frac{1/Q_m}{1/Q} \approx \frac{3 \ln(h_e/a) \ln(L/2r)}{2\theta L/2r} \quad (18)$$

For tip 7 (which has a 181 nm radius, $h_e \sim 1 \mu\text{m}$, contact angle ~ 1 rad) inserted into pure water to a depth of 9 μm , the ratio is ~ 1.3 , giving a meniscus damping that is comparable to Stokes drag. If the needle radius is instead 30 nm, then the ratio of meniscus damping to drag force decreases to ~ 0.25 .

Some evidence in support of the model of meniscus damping is found by comparing the damping using tip 7 to damping using a 30 nm radius tip (tip 26). The tip is inserted (initially to a depth of $\sim 9 \mu\text{m}$) into a droplet of pure water, and Q is recorded at 5 s intervals. Rather than retracting the tip, the insertion depth changes are due to evaporation. Two relevant features were noted. First, for around a 9 μm insertion depth, while the damping was 31% lower for the smaller diameter tip, the peak-to-peak fluctuations of ~ 0.0001 were ~ 30 times smaller than those for the larger diameter needle. Second, beyond a point where we assume the meniscus has become pinned to the end of the needle, the damping

(28) Lide D. R. *CRC Handbook of Chemistry and Physics*; CRC Press: Boca Raton, FL, 2002.

(29) Gunnaes, A. E.; Karlsen, O. B.; Zagierski, P. T. *J. Alloys Compd.* **2000**, 297, 144.

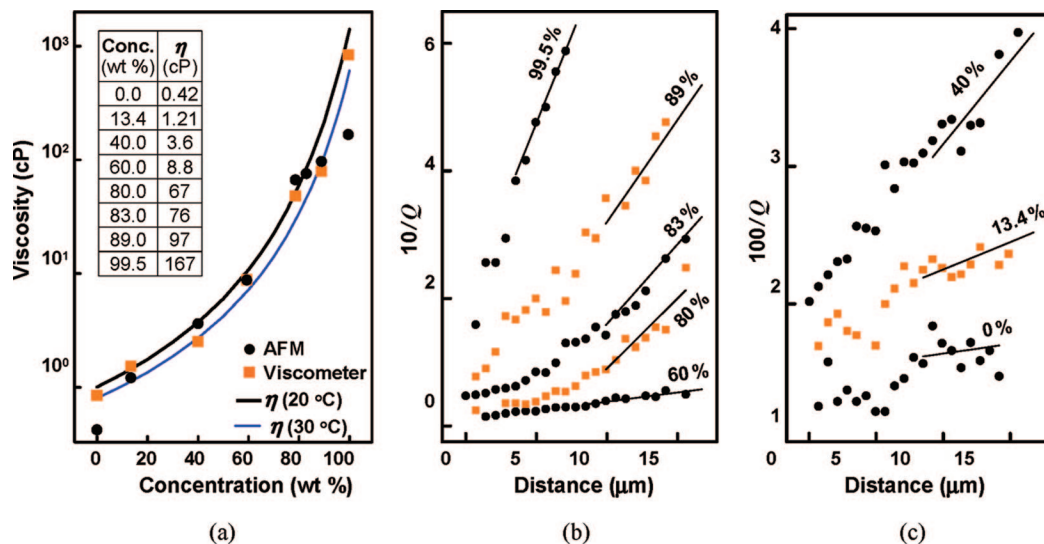


Figure 8. Viscosities of aqueous solutions of glycerol from measurements of damping ($1/Q$) as a function of insertion depth of tip 7 for a model of the Stokes drag on a slender cylinder. (a) Values of viscosity determined by the AFM measurements compared with measurements using a cone-and-plate viscometer and with published values.²⁸ The numerical values of AFM measured viscosity also are reported in the inset table using the viscosity at 60 wt % as measured by the viscometer as the reference value of viscosity. AFM measured damping as a function of insertion depth for solutions of (b) 60–99.5 wt % glycerol and (c) 0–40 wt % glycerol. The straight lines on each curve indicate the estimated slope that was used to calculate each value of viscosity. In panels b and c, in order to more clearly separate the data sets, the values of $1/Q$ are offset by 0.0025, 0.004, 0.01, and 0.03 for the 13.4, 40, 80, and 83 wt % solutions, respectively.

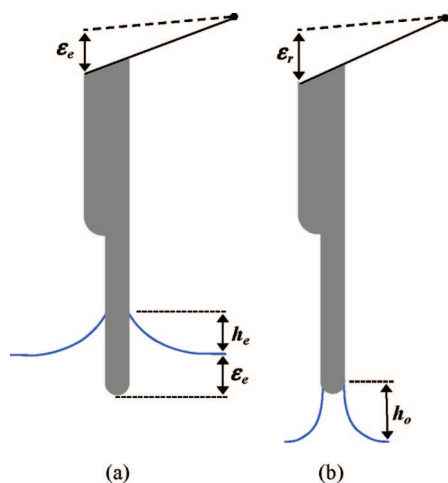


Figure 9. Schematic of offsets between the AFM scanner position and the needle-tip (a) ϵ_e at point ii and (b) ϵ_r at point v due to deflection of the cantilever by wetting force. Points ii and v are defined in Figure 4.

monotonically decreases to a level indistinguishable from the cantilever damping in air, prior to the needle breaking free from the liquid.

On the basis of eq 17 when L is less than h_e , $h = L$ in eq 17, and the meniscus damping decreases and vanishes for $L = a$. At this insertion depth, the meniscus becomes pinned on the end of the needle. Damping can occur as the meniscus is pulled higher, but the liquid is now mostly constrained in a much wider channel defined by the air–liquid interface of the meniscus, which should dramatically reduce shear rates and dissipation.

These correspondences between the experiment and the model are encouraging, but are only qualitative given the nonideal geometry of the measurement with the smaller diameter needle. Specifically, this needle was inserted near the edge of a water droplet that was receding laterally (as well as vertically due to evaporation).

Overall, the additional surface damping term, whatever its cause, can reduce the dynamic range of measuring the viscosity through Stokes drag. Alternatively, if the meniscus drag model is correct, since it also is proportional to viscosity, perhaps it can be used to determine viscosity without needing to insert the needles to the large depths required for Stokes drag to dominate.

f. Potential for Improved Measurement Accuracy and Sensitivity. The needle-tipped probes provided measurements of several properties, usually yielding results that were smaller than 10% RSD and 10% RD from accepted values. This degree of accuracy was possible with very limited environmental control. This level of accuracy appears to be adequate for purposes of correlating results from in situ AFM processing of liquids with measurements of dimensionless parameters (e.g., the processing parameter in eq 10). Tighter environmental control of temperature, relative humidity, and vapor pressure would likely improve accuracy. Additionally, structural and chemical defects on the needles that introduce pinning of the liquids might be reduced by overcoating the needles with an appropriate coating. For example, a polymer coating can be smoothed further by annealing at elevated temperatures that are still well below melting point of the Ag_2Ga needles (which is over 600 °C.²⁹) Lower cantilever stiffness than used in the study may also be used to magnify small fluctuations (e.g., those due to small pinning defects, differences in advancing and receding contact angle, and van der Waals forces just prior to snap in of the needle into the liquid). Stiffer cantilevers generally have large values of Q and could be used to increase the dynamic range of Q -damping measurements. Simultaneous Q damping and $F-D$ measurements are technically feasible with current AFM systems but not implemented in the interface. Combination of these two modes could provide improved insight as to the exact location of the meniscus with respect to pinning points on the needle, which could help provide better insight into the role of the meniscus on damping. The limits of the experimental measurement procedures can be further controlled and examined using nonvolatile, nonoxidizing oils such as low molecular weight poly(dimethylsiloxane) (PDMS) or poly(fluoromethylalkylsiloxane) (PFAS).

6. Conclusions

Long, constant diameter nanoneedles and dual-diameter nanoneedles have been demonstrated to enable reasonably repeatable and interpretable AFM measurements of several material properties of liquids. In these first attempts at these measurements, generally good agreement is found with traditional measurement procedures and published reports. For most measurements, the data are fairly easy to collect, and the probe can survive a number of measurements without damage. Note that only two probes (tips 6 and 7) were used to collect the entire set of data in Tables 2 and 3, and Figures 5 and 8. This included repeated rinsing of the probes to remove any possible depositions of materials from the solutions, repeated examinations in the SEM, and repeated loadings of the probes into the AFM cantilever holder.

In conclusion, these needle-tipped AFM probes provide very detailed information about the properties of liquids quickly, and potentially interactively, which supports future potential applications of combined in situ measurement, manipulation, and processing of liquids in ultrasmall reservoirs. Among AFM probes, the unique stair-step features appears especially useful for helping to delineate subtle and fundamentally interesting molecular interactions between liquid–solid interface. While reasonable accuracy has been demonstrated for measuring macroscopic properties of liquids for purposes of materials processing, continued studies with the needles are likely to lead to improved accuracy and repeatability, needed to more clearly sense the fundamental molecular properties.

Acknowledgment. This study was partially supported by National Science Foundation Grant ECS-0506941 and National Aeronautics and Space Administration cooperative agreement NCC5-571. Specific advice and insight from G. McKinley of MIT on meniscus height and principles of wetting is greatly appreciated.

Appendix A: Correction of the Model of the $F-D$ Curve for Cantilever Deflections

The model presented in Section 2 for interpreting the $F-D$ curves of liquids assumed the cantilever deflection is negligible, or that the cantilever is essentially rigid. For a rigid cantilever, the position reported by the z -scan motor (the horizontal axis on the $F-D$ curve) is identical to the position of the cantilever tip. For a nonrigid cantilever, the tip position is offset from the z -scan position by changes in force. Between point i and point ii (in Figure 4), the change in force F_e produces a position offset $\epsilon_e = F_e/k$ per eq 5 and as illustrated in Figure 9a. This offset modifies the expression for eq 5 as

$$h_e = H - d - (F_e/k) \quad (5a)$$

Between point v and point vi , the force changes by F_r corresponding to a change in cantilever deflection $\epsilon_r = F_r/k$. Per Figure 9b, the meniscus height at point v is modified to

$$h_o = c + \Delta - \delta - (F_r/k) \quad (8a)$$

The reported values of meniscus height calculated by scheme 2 include the corrections indicated in eqs 5a and 8a and are considered in the data reported in Figure 6 and Table 4. For a cantilever with spring constant of 2 N/m, these offsets can become noticeable for a 100 nm diameter tip (11.3 nm in water, zero contact angle) and quite noticeable for a 1 μm diameter tip (113 nm), and considerably larger when using other cantilevers that have much smaller spring constants.

An additional position offset that may be included but was found to be negligible in the measurements reported here is the offset caused by van der Waals force. For a cantilever with spring constant of 4 N/m, the force would cause the needle to spontaneously wet at distances, for diameters between 0.1 and 1 μm , 0.5–1.1 nm closer than the presumed zero reference point shown in Figure 4.^{14,27}

LA802820U